

# Drift Identification for Lévy alpha-Stable Stochastic Systems

Harish S. Bhat

HBHAT@UCMERCED.EDU

Department of Applied Mathematics, University of California, Merced, 5200 N. Lake Rd, Merced, CA 95343

## Abstract

This paper focuses on a stochastic system identification problem: given time series observations of a stochastic differential equation (SDE) driven by Lévy  $\alpha$ -stable noise, estimate the SDE's drift field. For  $\alpha$  in the interval  $[1, 2)$ , the noise is heavy-tailed, leading to computational difficulties for methods that compute transition densities and/or likelihoods in physical space. We propose a Fourier space approach that centers on computing time-dependent characteristic functions, i.e., Fourier transforms of time-dependent densities. Parameterizing the unknown drift field using Fourier series, we formulate a loss consisting of the squared error between predicted and empirical characteristic functions. We minimize this loss with gradients computed via the adjoint method. For a variety of one- and two-dimensional problems, we demonstrate that this method is capable of learning drift fields in qualitative and/or quantitative agreement with ground truth fields.

## 1. Introduction

Consider a stochastic differential equation driven by Lévy  $\alpha$ -stable noise:

$$d\mathbf{X}_t = \mathbf{f}(\mathbf{X}_t)dt + G(\mathbf{X}_t)d\mathbf{L}_t. \quad (1)$$

Here  $\mathbf{X}_t$  is an  $\mathbb{R}^d$ -valued stochastic process,  $\mathbf{f} : \mathbb{R}^d \rightarrow \mathbb{R}^d$  is the drift function (a vector field),  $G : \mathbb{R}^d \rightarrow \mathbb{R}^{d \times d}$  is the diffusion function (a matrix field), and  $\mathbf{L}_t$  is a Lévy symmetric  $\alpha$ -stable process in  $\mathbb{R}^d$ . We define this process in detail below, but for the sake of intuition, we mention two special cases. When  $\alpha = 1$ , the  $\alpha$ -stable density is the Cauchy density,  $p(x) = (\pi(1 + x^2))^{-1}$ . When  $\alpha = 2$ , the  $\alpha$ -stable density is Gaussian. We focus entirely on  $\alpha \in [1, 2)$ , in which case increments of  $\mathbf{L}_t$  are heavy-tailed and have infinite variance.

Assume we have access to  $n_T$  trajectories, each of which comprises observations of the state of (1) at discrete times  $\{j\Delta t\}_{j=0}^N$ . Denote the  $k$ -th such trajectory by  $\mathbf{X}^k = \{\mathbf{X}_0^k, \mathbf{X}_1^k, \dots, \mathbf{X}_N^k\}$ ; then our data is  $\mathcal{D} = \{\mathbf{X}^k\}_{k=1}^{n_T}$ . Assume that the diffusion function  $G$  is given. *The system identification (or learning/inverse) problem we address is: Given trajectory data  $\mathcal{D}$ , estimate the drift  $\mathbf{f}$  in (1).*

We consider (1) because of its capacity to model systems in biology (Reynolds and Frye, 2007; La Cognata et al., 2010; Ohta et al., 2022), engineering (Simsekli et al., 2019; Tajmiriahi et al., 2021; Gan et al., 2021), and finance (Hurst et al., 1999; Carr and Wu, 2003; Cartea and Howison, 2009) that all feature heavy tails. Despite the increasing importance of Lévy processes in modeling complex phenomena, *system identification* for Lévy-driven SDE such as (1) has received far less attention than the corresponding problem for SDE driven by standard Brownian motion.

We parameterize  $\mathbf{f}$  using parameters  $\theta$ . Suppose we try to estimate  $\theta$  by maximizing the likelihood  $p(\mathcal{D} | \theta)$ . To do this directly, we would need the SDE's transition density  $p(\mathbf{X}_{n+1}^k | \mathbf{X}_n^k, \theta)$ , on a large enough spatial domain to capture our observations. While it is possible to numerically solve a Fokker-Planck-Kolmogorov-type equation to obtain transition densities for particular initial

conditions (Gao et al., 2016), it is not clear how to scale such methods to solve estimation/inference problems. Additionally, the numerical experiments of Fang et al. (2022) indicate that even when the transition density is known, maximizing the likelihood directly does not yield accurate estimates of the drift and/or diffusion functions.

*In this paper, we develop a simulation and estimation framework for (1) that resides entirely in Fourier space.* When  $\alpha = 1$ , the  $\alpha$ -stable characteristic function (i.e., Fourier transform of the density) is  $\psi(s) = \exp(-|s|)$ . A small grid in  $s$  space is sufficient to represent  $\psi(s)$  accurately. In contrast, to represent the Cauchy density  $p(x)$  accurately, we need a large grid in  $x$  space, especially if we wish to preserve the normalization  $\int_{\mathbb{R}} p(x) dx = 1$ . More generally, for  $\alpha < 2$ , because increments of the process  $\mathbf{L}_t$  have heavy tails, we expect densities of the solution  $\mathbf{X}_t$  of (1) to decay to zero *slowly* as  $\|\mathbf{x}\| \rightarrow \infty$ . By Fourier duality, if the density is delocalized in space, then its Fourier transform must be localized in Fourier space (Mallat, 2008, Chap. 2). *By staying in Fourier space, we aim for both computational tractability and accurate simulation/estimation.*

Let us review prior studies that address system identification problems for (1). In the *parametric* version of the problem, the drift  $\mathbf{f}$  and diffusion  $G$  are specified up to a finite-dimensional set of parameters that one seeks to learn. Hongwei (2010) and Long et al. (2017) address the parametric problem using least squares estimators, while Jasra et al. (2019) pursues a Bayesian approach.

In the *nonparametric* problem, the goal is to learn the functional form of  $\mathbf{f}$ , and possibly that of  $G$  as well. Early work on this problem focuses on the high-frequency setting in which the time between observations tends to zero (Schmisser, 2014). For versions of the problem in which data is sampled regularly in time, a variety of modern methods have recently been applied, including Koopman operators (Lu and Duan, 2020), nonlocal Kramers-Moyal expansions (Li and Duan, 2021, 2022), normalizing flows (Lu et al., 2022; Li et al., 2022), minimization of a Kullback-Leibler loss with Fokker-Planck constraints (Dai et al., 2022), and neural networks (Chen et al., 2021; Wang et al., 2022; Fang et al., 2022). These approaches all work in physical space, necessitating approximations and/or ad hoc techniques to render the problem tractable. Note that time-dependent characteristic functions have been used to understand problems *other* than system identification for Lévy-driven SDE. We review this literature in Section 5.1 of the Appendix.

To our knowledge, no prior work on system identification considers recasting in Fourier space the equations of motion, the loss function, and/or the representation of unknown fields. In the present work, we show that a relatively unsophisticated Fourier space method can still successfully identify drifts in SDE driven by Cauchy noise, e.g., (1) with  $\alpha = 1$ . For periodic vector fields, we obtain quantitative agreement between learned and true drifts. For non-periodic polynomial vector fields, we obtain quantitative agreement in  $d = 1$  and qualitative agreement in  $d = 2$ . Taken together, these results approach the limits of prior methods.

## 2. Forward Problem

Throughout this work, we use boldface lowercase letters for vectors/vector fields; boldface uppercase letters for vector-valued random variables and stochastic processes; and standard uppercase letters for matrices. We think of vectors  $\mathbf{a}, \mathbf{b} \in \mathbb{R}^d$  as columns, so that  $\mathbf{a}^T \mathbf{b}$  is a scalar; here  $^T$  denotes transpose.

Let  $p(\mathbf{x}, t)$  denote the probability density function (PDF) of the exact solution  $\mathbf{X}_t$  of (1). Then the forward problem is: *Given  $p(\mathbf{x}, 0)$ , compute  $p(\mathbf{x}, t)$  for  $t > 0$ .* To solve the forward problem, we must introduce a few mathematical notions. Given any  $\mathbb{R}^d$ -valued random variable  $\mathbf{X}$  with density

$p(\mathbf{x})$ , we can define the characteristic function as the Fourier transform of the density:

$$\psi(\mathbf{s}) = \widehat{p}(\mathbf{s}) = E[e^{i\mathbf{s}^T \mathbf{X}}] = \int_{\mathbf{x} \in \mathbb{R}^d} e^{i\mathbf{s}^T \mathbf{x}} p(\mathbf{x}) d\mathbf{x}. \quad (2)$$

A random variable is determined by its characteristic function, and characteristic functions (unlike, e.g., moment-generating functions) can be used to distinguish numerically between random variables with different distributions (McCullagh, 1994; Waller, 1995; Luceño, 1997). Note that

$$\psi(\mathbf{0}) = \int_{\mathbf{x} \in \mathbb{R}^d} p(\mathbf{x}) d\mathbf{x} = 1. \quad (3)$$

Returning to definitions: let  $L_t^j$  denote the  $j$ -th component of  $\mathbf{L}_t \in \mathbb{R}^d$ . Here we assume that, for  $j \neq k$ ,  $L_t^j$  and  $L_t^k$  are independent scalar  $\alpha$ -stable Lévy processes defined by the following criteria: (i)  $L_0^j = 0$  almost surely, (ii)  $L_t^j$  has independent increments, and (iii) For  $t_2 > t_1 \geq 0$ ,  $L_{t_2}^j - L_{t_1}^j$ , the increment over a time interval of length  $t_2 - t_1$ , has an  $\alpha$ -stable distribution with scale parameter  $\sigma = (t_2 - t_1)^{1/\alpha}$ , skewness parameter  $\beta = 0$ , and location parameter  $\mu = 0$ .

The term  $d\mathbf{L}_t$  in SDE (1) is shorthand for an increment of the  $\mathbf{L}_t$  process over a time interval  $dt$ ; for further details, consult Applebaum (2009). For our purposes, it is sufficient to work with the Euler-Maruyama temporal discretization of (1) (Janicki and Weron, 1994):

$$\mathbf{x}_{n+1} = \mathbf{x}_n + \mathbf{f}(\mathbf{x}_n)h + G(\mathbf{x}_n)\Delta\mathbf{L}_{n+1}. \quad (4)$$

The random vector  $\Delta\mathbf{L}_{n+1}$ , which is independent of  $\mathbf{x}_n$ , consists of independent increments of  $\alpha$ -stable processes all over a time interval  $h$ . Therefore, its characteristic function is

$$\psi_{\Delta\mathbf{L}_{n+1}}(\mathbf{s}) = \prod_{j=1}^d \exp(-h|s_j|^\alpha). \quad (5)$$

Let  $\tilde{p}(\mathbf{x}, t_{n+1})$  denote the PDF of  $\mathbf{x}_{n+1}$ . Let us denote the conditional density of  $\mathbf{x}_{n+1}$  given  $\mathbf{x}_n = \mathbf{y}$  by  $p_{n+1,n}(\mathbf{x}|\mathbf{y})$ . Marginalization yields an evolution equation for the marginal density of  $\mathbf{x}_n$ :

$$\tilde{p}(\mathbf{x}, t_{n+1}) = \int_{\mathbf{y} \in \mathbb{R}^d} p_{n+1,n}(\mathbf{x}|\mathbf{y}) \tilde{p}(\mathbf{y}, t_n) d\mathbf{y}. \quad (6)$$

Assume that  $G(\mathbf{y}) = \text{diag } \mathbf{g}(\mathbf{y})$ . Computing the characteristic function of both sides, we obtain

$$\psi_{n+1}(\mathbf{s}) = \int_{\mathbf{y} \in \mathbb{R}^d} e^{i\mathbf{s}^T(\mathbf{y} + \mathbf{f}(\mathbf{y})h) - h|\mathbf{s}^T \mathbf{g}(\mathbf{y})|^\alpha} \tilde{p}(\mathbf{y}, t_n) d\mathbf{y}. \quad (7)$$

To derive this, we start from (5) and build up the right-hand side of (4), conditional on  $\mathbf{x}_n = \mathbf{y}$ . Scaling  $\Delta\mathbf{L}_{n+1}$  by  $G(\mathbf{y}) = \text{diag } \mathbf{g}(\mathbf{y})$  yields the characteristic function  $\exp(-h|\mathbf{s}^T \mathbf{g}(\mathbf{y})|^\alpha)$ . Translation by  $\mathbf{y} + \mathbf{f}(\mathbf{y})h$  yields the prefactor  $\exp(i\mathbf{s}^T(\mathbf{y} + \mathbf{f}(\mathbf{y})h))$ . Putting these pieces together gives (7). Applying the inverse transform  $\tilde{p}(\mathbf{y}, t_n) = (2\pi)^{-d} \int_{\mathbf{u} \in \mathbb{R}^d} e^{-i\mathbf{u}^T \mathbf{y}} \psi_n(\mathbf{u}) d\mathbf{s}$ , we obtain

$$\psi_{n+1}(\mathbf{s}) = \int_{\mathbf{u} \in \mathbb{R}^d} \tilde{K}(\mathbf{s}, \mathbf{u}) \psi_n(\mathbf{u}) d\mathbf{u} \quad (8a)$$

$$\tilde{K}(\mathbf{s}, \mathbf{u}) = \frac{1}{(2\pi)^d} \int_{\mathbf{y} \in \mathbb{R}^d} e^{i\mathbf{s}^T(\mathbf{y} + \mathbf{f}(\mathbf{y})h) - h|\mathbf{s}^T \mathbf{g}(\mathbf{y})|^\alpha - i\mathbf{u}^T \mathbf{y}} d\mathbf{y}. \quad (8b)$$

It may seem as though we can directly apply quadrature to evaluate (8b) and thereby obtain numerical methods to track the time-evolution of the characteristic function. However, note that in the  $h \rightarrow 0$  limit, the kernel  $\tilde{K}(\mathbf{s}, \mathbf{u})$  becomes  $\delta(\mathbf{s} - \mathbf{u})$ . For  $h > 0$  sufficiently small, typical quadrature methods cannot handle the nearly singular nature of (8b). To cope, we Taylor expand  $\tilde{K}$  in the time step  $h$ . We present the derivation for the special case when  $\mathbf{g}(\mathbf{y}) = \mathbf{g}$ , a constant vector:

$$\begin{aligned} \tilde{K}(\mathbf{s}, \mathbf{u}) &= \frac{1}{(2\pi)^d} \int_{\mathbf{y} \in \mathbb{R}^d} e^{i(\mathbf{s}-\mathbf{u})^T \mathbf{y}} e^{h(is^T \mathbf{f}(\mathbf{y}) - |\mathbf{s}^T \mathbf{g}(\mathbf{y})|^\alpha)} d\mathbf{y} = \frac{e^{-h|\mathbf{s}^T \mathbf{g}|^\alpha}}{(2\pi)^d} \int_{\mathbf{y} \in \mathbb{R}^d} e^{i(\mathbf{s}-\mathbf{u})^T \mathbf{y}} e^{his^T \mathbf{f}(\mathbf{y})} d\mathbf{y} \\ &= \frac{1}{(2\pi)^d} e^{-h|\mathbf{s}^T \mathbf{g}|^\alpha} \int_{\mathbf{y} \in \mathbb{R}^d} e^{i(\mathbf{s}-\mathbf{u})^T \mathbf{y}} \left[ 1 + his^T \mathbf{f}(\mathbf{y}) - \frac{h^2}{2} (\mathbf{s}^T \mathbf{f}(\mathbf{y}))^2 + O(h^3) \right] d\mathbf{y} \\ &\approx e^{-h|\mathbf{s}^T \mathbf{g}|^\alpha} \left[ \delta(\mathbf{s} - \mathbf{u}) + \frac{hi}{(2\pi)^d} \mathbf{s}^T \widehat{\mathbf{f}}(\mathbf{s} - \mathbf{u}) - \frac{h^2}{2(2\pi)^d} \mathbf{s}^T \widehat{\mathbf{f}\mathbf{f}^T}(\mathbf{s} - \mathbf{u}) \mathbf{s} \right] \end{aligned} \quad (9)$$

To justify truncation of the above expansion at second-order in  $h$ , we note that the Euler-Maruyama discretization (4) itself has  $O(h^2)$  local truncation error. For examples of characteristic function evolution (8a) and kernel expansion (9), see Section 5.2 of the Appendix.

The expansion (9) extracts and exposes the  $\delta$  singularity. As we will only use (9) under the integral in (8a), the integral against  $\delta(\mathbf{s} - \mathbf{u})$  yields a contribution of  $\psi_n(\mathbf{s})$ . With the  $\delta$  singularity out of the way, we can treat the rest of the integral in a number of ways.

While the derivation can easily be extended to the case where  $\mathbf{g}(\mathbf{y})$  is not constant in  $\mathbf{y}$ , we leave a complete exploration of that version of the method (including numerical results) for future work. For the remainder of the present work, we assume that  $\mathbf{g}$  is a known, constant vector. We focus on applying (9) and (8a) to the problem of identifying the drift  $\mathbf{f}$ . Note that combining (9) and (8a) yields the following discrete-time, continuous-space *characteristic function evolution* equation:

$$\psi_{n+1}(\mathbf{s}) = e^{-h|\mathbf{s}^T \mathbf{g}|^\alpha} \left[ \psi_n(\mathbf{s}) + \int_{\mathbf{u} \in \mathbb{R}^d} \left( \frac{hi}{(2\pi)^d} \mathbf{s}^T \widehat{\mathbf{f}}(\mathbf{s} - \mathbf{u}) \psi_n(\mathbf{u}) - \frac{h^2}{2(2\pi)^d} \mathbf{s}^T \widehat{\mathbf{f}\mathbf{f}^T}(\mathbf{s} - \mathbf{u}) \mathbf{s} \psi_n(\mathbf{u}) \right) d\mathbf{u} \right]. \quad (10)$$

### 3. System Identification

Here we address the system identification problem described in Section 1. To begin, assume that  $\mathbf{f}$  is parameterized by  $\boldsymbol{\theta}$ —we detail this below. We will estimate  $\boldsymbol{\theta}$  by minimizing a loss function that consists of the squared difference between predicted and empirical characteristic functions. To unpack this, first note that each trajectory gives rise to a time-dependent empirical density consisting of a sequence of point masses: for  $j = 0, 1, \dots, N$ ,  $\tilde{p}^k(\mathbf{x}, t_j) = \delta(\mathbf{x} - \mathbf{X}_j^k)$ . Averaging over all  $n_T$  trajectories and applying the Fourier transform (2), we obtain the *empirical characteristic function* of our collection of trajectories: for  $j = 0, 1, \dots, N$ ,

$$\tilde{\psi}(\mathbf{s}, t_j) = \frac{1}{n_T} \sum_{k=1}^{n_T} \exp(is^T \mathbf{X}_j^k). \quad (11)$$

Now fix  $j \in [0, \dots, N-1]$ . Let  $h = \Delta t/\nu$  for some integer  $\nu \geq 1$  sufficiently large so that (10) is stable and accurate. Take (11) as the *initial condition*  $\psi_0(\mathbf{s})$  for the evolution equation (10). Given

parameters  $\boldsymbol{\theta}$  that determine  $\mathbf{f}$ , we iterate (10) for  $\nu$  steps. We obtain a *predicted* characteristic function corresponding to time  $t_{j+1}$  in our data set—let us denote it as  $\psi(\mathbf{s}, t_{j+1}; \boldsymbol{\theta})$ . We then form

$$\Lambda_{\mathcal{C}}(\boldsymbol{\theta}) = \frac{1}{2} \sum_{j=0}^{N-1} \int_{\mathbf{s} \in \mathbb{R}^d} \left\| \psi(\mathbf{s}, t_{j+1}; \boldsymbol{\theta}) - \tilde{\psi}(\mathbf{s}, t_{j+1}) \right\|^2 d\mathbf{s}. \quad (12)$$

A key feature of the loss  $\Lambda_{\mathcal{C}}(\boldsymbol{\theta})$  is that it does not require the evaluation of any probability density functions in real space. To put it another way, we can compute (12) without computing the inverse Fourier transforms of our predicted characteristic functions. This is contrast to, for instance, loss functions based on the negative log likelihood. Especially for  $\alpha$  near 1, we expect that predicted densities (equivalently, inverse Fourier transforms of predicted characteristic functions) will require massive spatial domains to capture heavy-tailed behavior. We prefer to stay in Fourier space.

Note that the loss (12) is a special case of the *maximum mean discrepancy* (MMD) loss, which has been used in other areas of machine learning (Chwialkowski et al., 2015; Muandet et al., 2017). We have not seen (12) used before in system identification problems.

**Representation/Parameterization of the Drift Field.** Let  $\phi_m$  denote the  $m$ -th component of a vector field  $\phi$ . Assume there exists an integer  $L > 0$  such that  $\phi_m \in \mathcal{L}^2([-L\pi, L\pi]^d, \mathbb{R})$  for all  $m$ . Then the Fourier series expansion of  $\phi$  converges in  $\mathcal{L}^2$  to  $\phi$ . By choosing  $L$  sufficiently large, we can use Fourier series to represent many well-behaved  $\mathcal{L}^2$  vector fields.

Let  $J$  be a positive integer indicating how many Fourier modes we wish to use. Let  $\mathbf{j} = (j_1, \dots, j_d)$  be a multi-index, a vector of integers. Let  $\mathcal{J} = \{\mathbf{j} \in \mathbb{Z}^d \mid |j_\ell| \leq J \text{ for all } \ell\}$ . Then, for the  $m$ -th component of  $\mathbf{f}$ , our Fourier series model and its Fourier transform are:

$$f_m(\mathbf{x}; \boldsymbol{\theta}) = \sum_{\mathbf{j} \in \mathcal{J}} \theta_m^{\mathbf{j}} e^{i\mathbf{j}^T \mathbf{x}/L} \implies \hat{f}_m(\mathbf{s}) = (2\pi)^d \sum_{\mathbf{j} \in \mathcal{J}} \theta_m^{\mathbf{j}} \delta(\mathbf{s} + \mathbf{j}/L). \quad (13)$$

From (13),  $f_m(\mathbf{x})f_{m'}(\mathbf{x}) = \sum_{\mathbf{j}, \mathbf{j}' \in \mathcal{J}} \theta_m^{\mathbf{j}} \theta_{m'}^{\mathbf{j}'} e^{i(\mathbf{j}+\mathbf{j}')^T \mathbf{x}/L} = \sum_{\mathbf{k} \in \mathcal{K}} \sum_{\mathbf{j} \in \mathcal{J}} \theta_m^{\mathbf{j}} \theta_{m'}^{\mathbf{k}-\mathbf{j}} e^{i\mathbf{k}^T \mathbf{x}/L}$ , with  $\mathbf{k} = \mathbf{j} + \mathbf{j}'$  and  $\mathcal{K} = \{\mathbf{k} \in \mathbb{Z}^d \mid |k_m| \leq 2J \text{ for all } m\}$ . Then the Fourier transform is

$$\widehat{f_m f_{m'}}(\mathbf{s}) = (2\pi)^d \sum_{\mathbf{k} \in \mathcal{K}} \left[ \sum_{\mathbf{j} \in \mathcal{J}} \theta_m^{\mathbf{j}} \theta_{m'}^{\mathbf{k}-\mathbf{j}} \right] \delta(\mathbf{s} + \mathbf{k}/L) \quad (14)$$

Using (13), (14), and the definition  $(\boldsymbol{\theta} * \boldsymbol{\theta}^T)^{\mathbf{k}} = \sum_{\mathbf{j} \in \mathcal{J}} \theta^{\mathbf{j}} (\theta^{\mathbf{k}-\mathbf{j}})^T$ , we obtain

$$\hat{\mathbf{f}}(\mathbf{s}) = (2\pi)^d \sum_{\mathbf{j} \in \mathcal{J}} \boldsymbol{\theta}^{\mathbf{j}} \delta(\mathbf{s} + \mathbf{j}/L), \quad \text{and} \quad \widehat{\mathbf{f}\mathbf{f}^T}(\mathbf{s}) = (2\pi)^d \sum_{\mathbf{k} \in \mathcal{K}} (\boldsymbol{\theta} * \boldsymbol{\theta}^T)^{\mathbf{k}} \delta(\mathbf{s} + \mathbf{k}/L). \quad (15)$$

**Forward Propagation.** Substituting (15) into (10), we derive

$$\psi_{k+1}(\mathbf{s}) = e^{-h|\mathbf{s}^T \mathbf{g}|^\alpha} \left[ \psi_k(\mathbf{s}) + i h \mathbf{s}^T \sum_{\mathbf{j} \in \mathcal{J}} \boldsymbol{\theta}^{\mathbf{j}} \psi_k(\mathbf{s} + \mathbf{j}/L) - \frac{h^2}{2} \mathbf{s}^T \left( \sum_{\mathbf{k} \in \mathcal{K}} (\boldsymbol{\theta} * \boldsymbol{\theta}^T)^{\mathbf{k}} \psi_k(\mathbf{s} + \mathbf{k}/L) \right) \mathbf{s} \right]. \quad (16)$$

By choosing a Fourier representation of  $\mathbf{f}$ , we have ensured that the transforms  $\hat{\mathbf{f}}$  and  $\widehat{\mathbf{f}\mathbf{f}^T}$  involve Dirac deltas, enabling the exact evaluation of the integrals in (10). Had we chosen other representations of  $\mathbf{f}$ —e.g., polynomials, splines, or neural networks—we would have had to evaluate the

integrals in (10) via numerical quadrature. This and the  $\mathcal{L}^2$  property mentioned above is why we employ a Fourier series representation of  $\mathbf{f}$ .

To finally bring (16) into a form suitable for numerical implementation, we must discretize the spatial variable  $\mathbf{s}$ . Here we track the pointwise values of  $\psi$  on an equispaced grid in  $\mathbf{s}$  space, as in a finite-difference method. Based on the form of (16), we choose a grid with spacing  $\Delta s = 1/(n_L L)$  for some integer  $n_L \geq 1$ . The grid itself can be described by the collection of points  $\mathcal{M} = \{\mathbf{j}\Delta s \mid |j_\ell| \leq M \text{ for all } \ell\}$ . Then evaluating both sides of (16) at an arbitrary grid point  $\mathbf{j}\Delta s \in \mathcal{M}$ , we obtain the following fully discrete (in space and time) scheme:

$$\begin{aligned} \psi_{k+1}(\mathbf{j}\Delta s) = e^{-h\Delta s|\mathbf{j}^T \mathbf{g}|^\alpha} & \left[ \psi_k(\mathbf{j}\Delta s) + i(h\Delta s)\mathbf{j}^T \sum_{\mathbf{k} \in \mathcal{J}} \boldsymbol{\theta}^{\mathbf{k}} \psi_k((\mathbf{j} + \mathbf{k}n_L)\Delta s) \right. \\ & \left. - \frac{(h\Delta s)^2}{2} \mathbf{j}^T \left( \sum_{\mathbf{k} \in \mathcal{K}} (\boldsymbol{\theta} * \boldsymbol{\theta}^T)^{\mathbf{k}} \psi_k((\mathbf{j} + \mathbf{k}n_L)\Delta s) \right) \mathbf{j} \right] \end{aligned} \quad (17)$$

With the assumption that  $\psi_k(\ell\Delta s) = 0$  for any  $\ell\Delta s \notin \mathcal{M}$ , this gives us a closed system of equations to evolve  $\psi_k$  forward in time, on the spatial grid  $\mathcal{M}$ , starting from an initial condition  $\psi_0$ .

Note that (17) automatically preserves the normalization of the densities associated to each characteristic function. To see this, evaluate both sides of (17) at  $\mathbf{j} = \mathbf{0}$  to obtain  $\psi_{k+1}(\mathbf{0}) = \psi_k(\mathbf{0})$ . If the initial condition satisfies  $\psi_0(\mathbf{0}) = 1$ , then  $\psi_k(\mathbf{0}) = 1$  for all  $k \geq 0$ . By (3), the associated densities are all properly normalized. For additional remarks on the accuracy and stability of (16), see Section 5.3 in the Appendix.

**Adjoint Method.** Spatially discretizing (12) on the grid  $\mathcal{M}$  described above, we derive

$$\Lambda(\boldsymbol{\theta}) = \frac{1}{2} \sum_{j=0}^{N-1} \sum_{\mathbf{j} \in \mathcal{M}} \left\| \psi(\mathbf{j}\Delta s, t_{j+1}; \boldsymbol{\theta}) - \tilde{\psi}(\mathbf{j}\Delta s, t_{j+1}) \right\|^2. \quad (18)$$

We omit a factor of  $(\Delta s)^d$  as it plays no role in what follows. Our goal is to minimize the discrete-space, discrete-time loss (18) subject to the dynamics (17). This is akin to an optimal control problem in which the drift vector field  $\mathbf{f}$  (parameterized by  $\boldsymbol{\theta}$ ) plays the role of the control. In Section 5.4 of the Appendix, we detail an adjoint method to solve this dynamically constrained minimization problem. The net result of this method is an efficient algorithm to compute  $\nabla_{\boldsymbol{\theta}} \Lambda$ .

We have coded Python functions that implement both the MMD loss function (18) and its gradient with respect to the parameters  $\boldsymbol{\theta}$ , computed via the adjoint method. We pass these functions to SciPy's trust region optimizer, making use of the Symmetric Rank-1 (SR1) quasi-Newton Hessian approximation method (Byrd et al., 1996). In all cases, we use an initial guess for  $\boldsymbol{\theta}$  consisting of an array of zeros.

## 4. Numerical Results

To test the method's ability to identify systems driven by Lévy  $\alpha$ -stable noise, we conduct tests with synthetic data sets. In each test, we use the Euler-Maruyama method to generate trajectories from systems with known drift and diffusion fields  $\mathbf{f}$  and  $\mathbf{g}$ . Using this data, we apply the characteristic function evolution and adjoint method described above to learn  $\boldsymbol{\theta}$ , Fourier coefficients of our estimated drift field  $\mathbf{f}$ . We detail our error metrics below; in all cases, the idea is to compare the



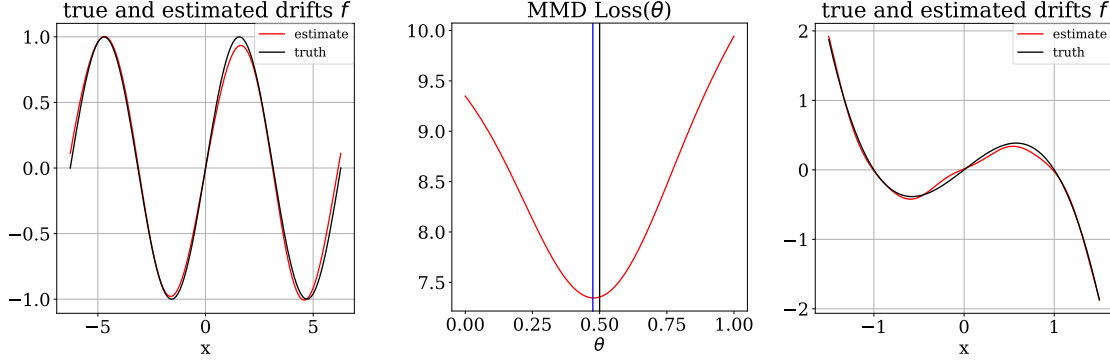


Figure 1: We plot results for  $\tilde{f}(x) = \sin x$  (left, middle) and  $\tilde{f}(x) = x - x^3$  (right). In the left and right plots, we plot the learned  $f$  (red) and true  $\tilde{f}$  (black). Note the close agreement.

estimated  $\mathbf{f}$  against the ground truth  $\tilde{\mathbf{f}}$ . We include particularly relevant implementation notes; for other implementation details, please consult Section 5.5 in the Appendix.

**One-Dimensional Vector Fields ( $d = 1$ ).** For all results in this section, we set  $\alpha = 1$ , the most challenging case. We set the diffusion constant to be  $g = 0.25$ . All one-dimensional training data consists of  $n_T = 100$  trajectories, each with initial condition  $X_0 = 0$ ,  $\Delta t = 10^{-1}$  and length  $N = 41$ . We set  $\nu = 100$  so that our method’s internal time step is  $h = \Delta t/\nu = 10^{-3}$ .

For our first one-dimensional test, we generate data using the known vector field  $\tilde{f}(x) = \sin x$ . Using  $J = 4$  in our Fourier model, we apply the procedures from Section 3 to learn  $\theta \in \mathbb{C}^{2J+1}$ . In the left-most panel of Figure 1, we plot  $f$  and  $\tilde{f}$  in red and black, respectively, noting the close agreement between the two. Let  $\tilde{\theta}$  denote the Fourier coefficients for  $\tilde{f}$ . The mean absolute error (MAE) of  $\theta$  from  $\tilde{\theta}$  is less than  $3.2 \times 10^{-4}$ .

To better understand the MMD loss, we set up an auxiliary model  $\theta = \mathbf{H}(\theta)$  for scalar  $\theta$ . The purpose of  $\mathbf{H}$  is to populate all entries of  $\theta$  with zeros except for those corresponding to the  $j = \pm 2$  modes; we set the  $j = 2$  coefficient equal to  $i\theta$  and the  $j = -2$  coefficient equal to  $-i\theta$ . Note that  $\mathbf{H}(0.5) = \tilde{\theta}$ , the ground truth Fourier coefficient vector. In the middle panel of Figure 1, we have plotted  $\Lambda(\mathbf{H}(\theta))$ , the MMD loss (18) evaluated on this auxiliary model that depends on only one real scalar. Note that the MMD loss’ global minimum (blue vertical bar) is quite close to the ground truth value (red vertical bar). This helps to justify our use of the MMD loss.

Next, we consider  $\tilde{f}(x) = x - x^3$ , which is not periodic and does not have a sparse Fourier representation. We choose this to simulate a real-world situation in which we do not have prior knowledge regarding the optimal basis to use in our model  $f$ . With all hyperparameters as above, we learn  $\theta \in \mathbb{C}^{2J+1}$  with  $J = 16$ . In the right-most panel of Figure 1, we plot  $f$  and  $\tilde{f}$  in red and black, respectively. We note that the curves agree closely on the domain  $[-3/2, 3/2]$ . For further analysis of the errors in this case, please see Section 5.6 in the Appendix.

**Two-Dimensional Trigonometric Vector Fields ( $d = 2$ ).** We continue with the difficult  $\alpha = 1$  case. For the first two two-dimensional problems we consider, the training data consists of  $n_T = 100$  trajectories of length  $N = 101$  with  $\Delta t = 0.4$ . We set  $\nu = 4000$  so that our method’s internal time step is  $h = 10^{-4}$ . The diffusion vector is set to  $\mathbf{g} = (0.1, 0.1)$ .

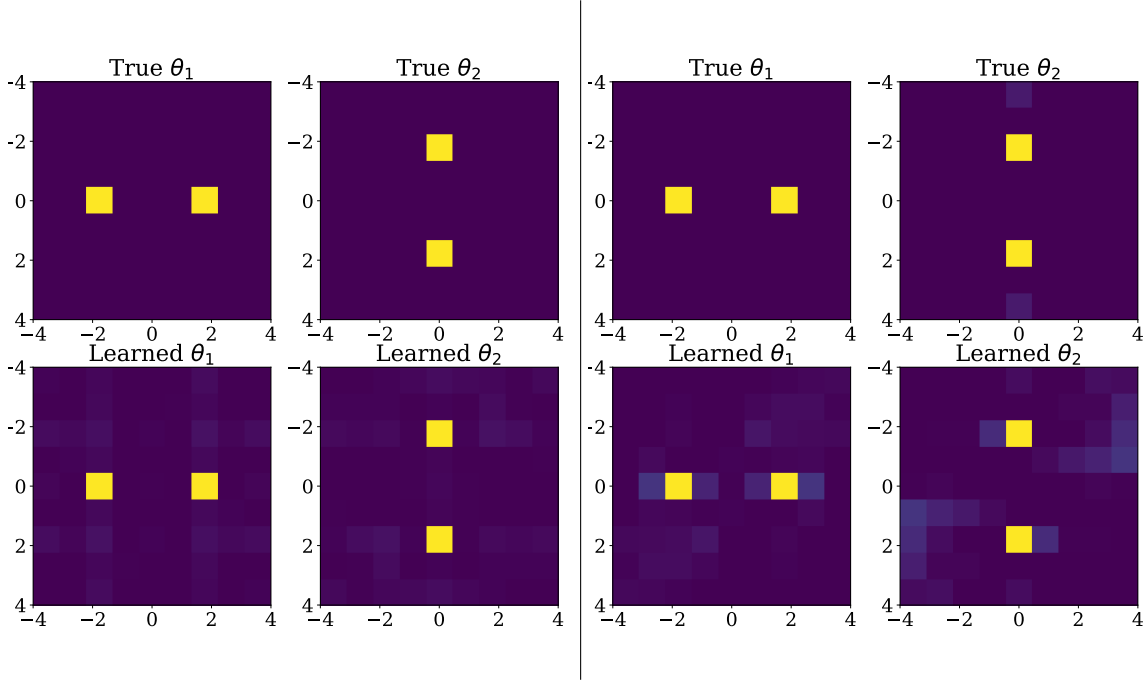


Figure 2: We plot true and learned results for  $\tilde{\mathbf{f}}(x_1, x_2) = (\sin x_2, -\sin x_1)$  (single well potential, left of the vertical bar) and  $\tilde{\mathbf{f}}(x_1, x_2) = (\sin x_2, -V'(x_1))$  with  $V(x) = ((\sin x/2)^2 - 4)^2/10$  (double well potential, right of the vertical bar). Each plot is a heatmap of  $|\theta_q|$ .

For data sets from two different ground truth  $\tilde{\mathbf{f}}$  fields (described below), we use our methods to estimate  $\theta$  with  $J = 4$ . Note that because  $d = 2$ , the complex array  $\theta$  is of size  $(2J + 1) \times (2J + 1) \times 2$ . In Figure 2, we use  $\theta_q$  as shorthand for  $\theta[:, :, q]$ , the matrix of two-dimensional Fourier series coefficients for the  $q$ -th component of the vector field  $\mathbf{f}$ . To avoid overfitting and to promote sparsity of  $\theta$ , we add an  $\mathcal{L}^1$  regularization term  $\mu \|\theta\|_1$  to our MMD loss, together with a corresponding subgradient of this term in our gradient function. We set  $\mu = 1$  and do not take any steps to optimize/tune this hyperparameter.

In Figure 2, we plot the true and learned results for  $\tilde{\mathbf{f}}(x_1, x_2) = (\sin x_2, -\sin x_1)$  (single well potential, left of the vertical bar) and  $\tilde{\mathbf{f}}(x_1, x_2) = (\sin x_2, -V'(x_1))$  with  $V(x) = ((\sin x/2)^2 - 4)^2/10$  (double well potential, right of the vertical bar). Each plot is a heatmap of  $|\theta_q|$ . Overall, we see close agreement between learned and true  $\theta$  matrices in each case. The MAE between learned and true Fourier coefficients is  $6.4 \times 10^{-5}$  (left) and  $6.2 \times 10^{-3}$  (right). As the true  $\theta_q$  matrices are highly sparse, we are confident that closer agreement is possible with our current setup, with a combination of more data and improved tuning of the hyperparameter  $\mu$ .

**Two-Dimensional Polynomial Vector Fields ( $d = 2$ ).** We now turn to two cases designed to challenge our current approach. In both cases, the true  $\tilde{\mathbf{f}}$  is polynomial in nature, yet we seek a Fourier model  $\mathbf{f}$ . Continuing with  $\alpha = 1$ , we consider the polynomial double-well potential  $V(x) = (x^2 - 4)^2/10$  and associated vector field with dissipation,  $\tilde{\mathbf{f}}(x_1, x_2) = (x_2, -V'(x_1) - x_1/4)$ .

In this case, we began with a set of  $n_T = 100$  trajectories each of length  $N = 41$  with  $\Delta t = 1.0$ . We set  $\nu = 100$  so that our method's internal time step is  $h = 10^{-2}$ . The diffusion vector is set



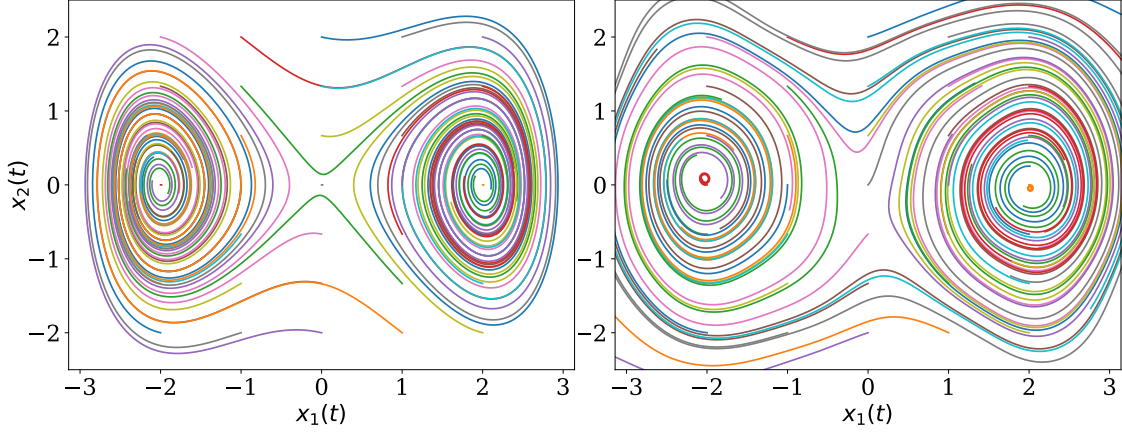


Figure 3: *Deterministic* phase portraits corresponding to the ground truth polynomial field  $\tilde{\mathbf{f}}(x) = (x_2, (2/5)x_1(4 - x_1^2) - x_1/4)$  (left) and learned Fourier model  $\mathbf{f}$  (right).

to  $\mathbf{g} = (0.1, 0.1)$ . Unlike the periodic two-dimensional vector fields above, this  $\tilde{\mathbf{f}}$  is unbounded, leading to trajectories with massive range in physical space. We restricted attention to trajectories that stayed within the box  $[-2\pi, 2\pi]^2$ , eliminating all but 29 of the 100 trajectories.

Because  $n_T = 29$  is a small number of trajectories, we did not obtain reasonable results using the *averaged* empirical characteristic function (11) as our target in the MMD loss. Hence we replaced (11) with  $\tilde{\psi}^k(\mathbf{s}, t_j) = \exp(is^T \mathbf{X}_j^k - (1/8)\mathbf{s}^T \mathbf{s})$  for each  $k = 1, \dots, n_T$ . Here each of the  $n_T$  trajectories is being treated as a target on its own, leading to one squared loss per trajectory. Averaging the resulting per-trajectory squared losses resulted in only superficial modifications to the loss (18) and associated adjoint method. Note also the dash of Gaussian regularization added to each empirical characteristic function, designed to force  $\tilde{\psi}^k$  to decay to zero. This improves performance of the characteristic function evolution method.

We set  $J = 8$  in our Fourier model  $\mathbf{f}$  and train. In Figure 3, we plot *deterministic* phase portraits for the ODE systems  $\dot{\mathbf{x}} = \tilde{\mathbf{f}}(\mathbf{x})$  (left, ground truth) and  $\dot{\mathbf{x}} = \mathbf{f}(\mathbf{x})$  (right, learned). We note that these vector fields are in qualitative agreement, with two stable fixed points located at approximately  $(\pm 2, 0)$  separated by a saddle near the origin. We believe that this qualitative agreement is sufficient for many purposes, e.g., using the identified system  $\mathbf{f}$  for prediction and/or control. These results were possible even with coarse temporal resolution in the training data ( $N = 41$  and  $\Delta t = 1.0$ ).

Next, we consider the Maier-Stein vector field  $\tilde{\mathbf{f}}(\mathbf{x}) = (x_1 - x_1^3 - x_1 x_2^2, -(1 + x_1^2)x_2)$ . We set  $\alpha = 1.5$  and  $\mathbf{g} = (1, 1)$  to match Fang et al. (2022). We began with a set of  $n_T = 100$  trajectories each of length  $N = 11$  with  $\Delta t = 1.0$ . We set  $\nu = 1000$  so that our method’s internal time step is  $h = 10^{-3}$ . Restricting attention to trajectories confined to  $[-2\pi, 2\pi]^2$ , we retained  $n_T = 58$  trajectories. As our target, we use the empirical characteristic functions  $\psi^k(\mathbf{s}, t_j) = \exp(is^T \mathbf{X}_j^k)$  for  $k = 1, \dots, n_T$ . As  $\alpha = 1.5$  and  $\mathbf{g} = (1, 1)$  in this case, we deemed it unnecessary to include a Gaussian regularization in  $\tilde{\psi}^k$ .

We again set  $J = 8$  in our Fourier model  $\mathbf{f}$  and train. In Figure 4, we plot *deterministic* phase portraits for the ODE systems  $\dot{\mathbf{x}} = \tilde{\mathbf{f}}(\mathbf{x})$  (left, ground truth) and  $\dot{\mathbf{x}} = \mathbf{f}(\mathbf{x})$  (middle, learned). Note

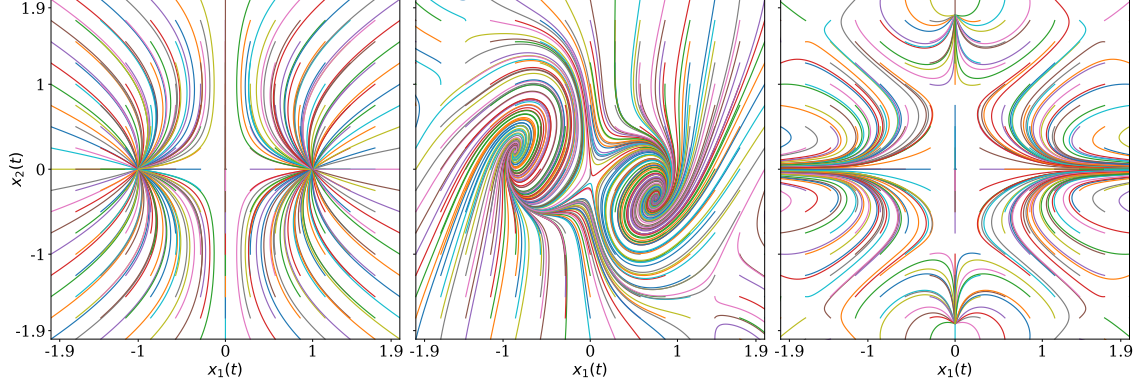


Figure 4: *Deterministic* phase portraits illustrating the ground truth Maier-Stein vector field  $\tilde{\mathbf{f}}(\mathbf{x}) = (x_1 - x_1^3 - x_1x_2^2, -(1 + x_1^2)x_2)$  (left), and two learned vector fields  $\mathbf{f}$ , one with no symmetries enforced (middle) and one with even/odd symmetries that match those of  $\tilde{\mathbf{f}}$  (right).

that even with the sparse-in-time training set, we learn a vector field with two stable fixed points located roughly near  $(\pm 1, 0)$  as in  $\tilde{\mathbf{f}}$ . Based on this experiment, we realized that  $\tilde{\mathbf{f}}$  enjoys symmetries that stem from the fact that  $\tilde{f}_1$  is odd in  $x_1$  and even in  $x_2$ , while  $\tilde{f}_2$  is even in  $x_1$  and odd in  $x_2$ . We modified the Fourier representation (13) to incorporate these symmetries. As before, this required only superficial changes to the loss (18) and associated adjoint method. Retraining, we obtain a vector field  $\mathbf{f}$  associated with the phase portrait on the far right of Figure 4. We now see improved agreement with the left panel in terms of the vertical separatrix at  $x = 0$  together with the shapes of the integral curves flowing into the  $y = 0$  axis.

Again, these results are possible even with coarse temporal resolution in the training data ( $N = 11$  and  $\Delta t = 1.0$ ). We conjecture that a more scalable implementation of our algorithm in the  $d = 2$  case, enabling us to increase the volume of training data and increase spatial discretization parameters such as  $L$ ,  $M$ , and  $J$ , will lead to improved learning of polynomial vector fields.

## 5. Conclusion

The characteristic function evolution method enables us to accurately and stably evolve Lévy  $\alpha$ -stable dynamical systems forward in time. When coupled with the MMD loss function and the adjoint method, we have an end-to-end method for system identification. In this paper, we derived the method for the first time and demonstrated its potential. When the ground truth field is periodic, we succeed in identifying it using our Fourier representation, even for two-dimensional systems in the challenging  $\alpha = 1$  (Cauchy noise) case. Learned vector fields can capture key qualitative features of ground truth polynomial vector fields. In future work, we plan to expand our method to incorporate other types of models for  $\mathbf{f}$ , e.g., polynomial and neural network models. It seems likely that by combining Fourier space ideas proposed in the present paper with modern techniques from the literature, one may derive still superior system identification methods. We hope the present work enables further research in this direction.

## Acknowledgments

This research was partially supported by NSF DMS-1723272, and also benefited from computational resources that include the Pinnacles cluster at UC Merced (supported by NSF OAC-2019144) and Nautilus, supported by the Pacific Research Platform (NSF ACI-1541349), CHASE-CI (NSF CNS-1730158), Towards a National Research Platform (NSF OAC-1826967), and the University of California Office of the President. The author expresses gratitude for discussions with Arnold D. Kim on an earlier version of the project, and conversations with Hua Hsu that motivated completion of the work.

## References

- G. Alotta and M. Di Paola. Probabilistic characterization of nonlinear systems under  $\alpha$ -stable white noise via complex fractional moments. *Physica A: Statistical Mechanics and its Applications*, 420:265–276, 2015. URL <http://doi.org/10.1016/j.physa.2014.10.091>.
- Gioacchino Alotta and Mario Di Paola. Einstein-Smoluchowsky equation handled by complex fractional moments. In *ICFDA’14 International Conference on Fractional Differentiation and Its Applications 2014*, pages 1–6, 2014. URL <http://doi.org/10.1109/ICFDA.2014.6967405>.
- David Applebaum. *Lévy Processes and Stochastic Calculus*. Cambridge University Press, 2009.
- Richard H. Byrd, Humaid Fayeze Khalfan, and Robert B. Schnabel. Analysis of a symmetric rank-one trust region method. *SIAM Journal on Optimization*, 6(4):1025–1039, 1996. URL <http://doi.org/10.1137/S1052623493252985>.
- Peter Carr and Liuren Wu. The finite moment log stable process and option pricing. *The Journal of Finance*, 58(2):753–777, 2003. URL <http://doi.org/10.1111/1540-6261.00544>.
- Alvaro Cartea and Sam Howison. Option pricing with Lévy-stable processes generated by Lévy-stable integrated variance. *Quantitative Finance*, 9(4):397–409, 2009. URL <https://doi.org/10.1080/14697680902748506>.
- Xiaoli Chen, Liu Yang, Jinqiao Duan, and George Em Karniadakis. Solving inverse stochastic problems from discrete particle observations using the Fokker–Planck equation and physics-informed neural networks. *SIAM Journal on Scientific Computing*, 43(3):B811–B830, 2021. URL <https://doi.org/10.1137/20M1360153>.
- Kacper P Chwialkowski, Aaditya Ramdas, Dino Sejdinovic, and Arthur Gretton. Fast two-sample testing with analytic representations of probability measures. In C. Cortes, N. Lawrence, D. Lee, M. Sugiyama, and R. Garnett, editors, *Advances in Neural Information Processing Systems*, volume 28. Curran Associates, Inc., 2015. URL <http://papers.nips.cc/paper/2015/hash/b571ecea16a9824023ee1af16897a582-Abstract.html>.
- Giulio Cottone. Statistics of nonlinear stochastic dynamical systems under Lévy noises by a convolution quadrature approach. *Journal of Physics A: Mathematical and Theoretical*, 44(18):185001, 2011. URL <http://doi.org/10.1088/1751-8113/44/18/185001>.

- Min Dai, Jinqiao Duan, Jianyu Hu, Jianghui Wen, and Xiangjun Wang. Variational inference of the drift function for stochastic differential equations driven by Lévy processes. *Chaos: An Interdisciplinary Journal of Nonlinear Science*, 32(6):061103, 2022. URL <http://doi.org/10.1063/5.0095605>.
- Alberto Di Matteo and Antonina Pirrotta. Path integral method for nonlinear systems under Levy white noise. *ASCE-ASME J Risk and Uncert in Engrg Sys Part B Mech Engrg*, 3(3), 06 2017. URL <http://doi.org/10.1115/1.4036703>. 030905.
- Mario Di Paola and Gioacchino Alotta. Path integral methods for the probabilistic analysis of nonlinear systems under a white-noise process. *ASCE-ASME J Risk and Uncert in Engrg Sys Part B Mech Engrg*, 6(4), 08 2020. URL <http://doi.org/10.1115/1.4047882>. 040801.
- Cheng Fang, Yubin Lu, Ting Gao, and Jinqiao Duan. An end-to-end deep learning approach for extracting stochastic dynamical systems with  $\alpha$ -stable Lévy noise. *Chaos: An Interdisciplinary Journal of Nonlinear Science*, 32(6):063112, 2022. URL <http://doi.org/10.1063/5.0089832>.
- Runze Gan, Bashar I Ahmad, and Simon J Godsill. Lévy state-space models for tracking and intent prediction of highly maneuverable objects. *IEEE Transactions on Aerospace and Electronic Systems*, 57(4), 2021. URL <http://doi.org/10.1109/TAES.2021.3088430>.
- Ting Gao, Jinqiao Duan, and Xiaofan Li. Fokker–Planck equations for stochastic dynamical systems with symmetric Lévy motions. *Applied Mathematics and Computation*, 278:1–20, 2016. URL <http://doi.org/10.1016/j.amc.2016.01.010>.
- Long Hongwei. Parameter estimation for a class of stochastic differential equations driven by small stable noises from discrete observations. *Acta Mathematica Scientia*, 30(3):645–663, 2010. URL [https://doi.org/10.1016/S0252-9602\(10\)60067-7](https://doi.org/10.1016/S0252-9602(10)60067-7).
- S.R Hurst, E Platen, and S.T Rachev. Option pricing for a logstable asset price model. *Mathematical and Computer Modelling*, 29(10):105–119, 1999. URL [http://doi.org/10.1016/S0895-7177\(99\)00096-5](http://doi.org/10.1016/S0895-7177(99)00096-5).
- Jean Jacod. The Euler scheme for Lévy driven stochastic differential equations: limit theorems. *The Annals of Probability*, 32(3):1830–1872, 2004. URL <http://doi.org/10.1214/009117904000000667>.
- Aleksander Janicki and Aleksander Weron. *Simulation and Chaotic Behavior of alpha-Stable Stochastic processes*. CRC Press, 1994.
- Ajay Jasra, Kengo Kamatani, and Hiroki Masuda. Bayesian inference for stable Lévy–driven stochastic differential equations with high-frequency data. *Scandinavian Journal of Statistics*, 46(2):545–574, 2019. URL <http://doi.org/10.1111/sjos.12362>.
- A. La Cognata, D. Valenti, A. A. Dubkov, and B. Spagnolo. Dynamics of two competing species in the presence of Lévy noise sources. *Phys. Rev. E*, 82:011121, Jul 2010. URL <http://doi.org/10.1103/PhysRevE.82.011121>.

- Siu Kwan Lam, Antoine Pitrou, and Stanley Seibert. Numba: A LLVM-Based Python JIT Compiler. In *Proceedings of the Second Workshop on the LLVM Compiler Infrastructure in HPC*, LLVM '15, New York, NY, USA, 2015. Association for Computing Machinery. ISBN 9781450340052. URL <http://doi.org/10.1145/2833157.2833162>.
- Yang Li and Jinqiao Duan. A data-driven approach for discovering stochastic dynamical systems with non-Gaussian Lévy noise. *Physica D: Nonlinear Phenomena*, 417:132830, 2021. URL <http://doi.org/10.1016/j.physd.2020.132830>.
- Yang Li and Jinqiao Duan. Extracting governing laws from sample path data of non-Gaussian stochastic dynamical systems. *Journal of Statistical Physics*, 186(2):1–21, 2022. URL <http://doi.org/10.1007/s10955-022-02873-y>.
- Yang Li, Yubin Lu, Shengyuan Xu, and Jinqiao Duan. Extracting stochastic dynamical systems with  $\alpha$ -stable Lévy noise from data. *Journal of Statistical Mechanics: Theory and Experiment*, 2022(2):023405, 2022. URL <https://doi.org/10.1088/1742-5468/ac4e87>.
- Hongwei Long, Chunhua Ma, and Yasutaka Shimizu. Least squares estimators for stochastic differential equations driven by small Lévy noises. *Stochastic Processes and their Applications*, 127(5):1475–1495, 2017. URL <http://doi.org/10.1016/j.spa.2016.08.006>.
- Yubin Lu and Jinqiao Duan. Discovering transition phenomena from data of stochastic dynamical systems with Lévy noise. *Chaos: An Interdisciplinary Journal of Nonlinear Science*, 30(9):093110, 2020. URL <https://doi.org/10.1063/5.0004450>.
- Yubin Lu, Yang Li, and Jinqiao Duan. Extracting stochastic governing laws by non-local Kramers–Moyal formulae. *Philosophical Transactions of the Royal Society A: Mathematical, Physical and Engineering Sciences*, 380(2229):20210195, 2022. URL <https://doi.org/10.1098/rsta.2021.0195>.
- Alberto Luceño. Further evidence supporting the numerical usefulness of characteristic functions. *The American Statistician*, 51(3):233–234, 1997. URL <https://doi.org/10.1080/00031305.1997.10473968>.
- S. Mallat. *A Wavelet Tour of Signal Processing: The Sparse Way*. Elsevier Science, 2008.
- Peter McCullagh. Does the moment-generating function characterize a distribution? *The American Statistician*, 48(3):208–208, 1994. URL <http://doi.org/10.1080/00031305.1994.10476058>.
- Remigijus Mikulevicius and Changyong Zhang. On the rate of convergence of weak Euler approximation for nondegenerate SDEs driven by Lévy processes. *Stochastic Processes and their Applications*, 121(8):1720–1748, 2011. URL <http://doi.org/10.1016/j.spa.2011.04.004>.
- Krikamol Muandet, Kenji Fukumizu, Bharath Sriperumbudur, and Bernhard Schölkopf. Kernel mean embedding of distributions: A review and beyond. *Foundations and Trends in Machine Learning*, 10(1-2):1–141, 2017. URL <http://doi.org/10.1561/22000000060>.



- Morihiro Ohta, Toshitake Asabuki, and Tomoki Fukai. Intrinsic bursts facilitate learning of Lévy flight movements in recurrent neural network models. *Scientific Reports*, 12(1):1–10, 2022. URL <http://doi.org/10.1038/s41598-022-08953-z>.
- Andy M. Reynolds and Mark A. Frye. Free-flight odor tracking in *Drosophila* is consistent with an optimal intermittent scale-free search. *PLOS ONE*, 2(4):1–9, 04 2007. URL <http://doi.org/10.1371/journal.pone.0000354>.
- Emeline Schmisser. Non-parametric adaptive estimation of the drift for a jump diffusion process. *Stochastic Processes and their Applications*, 124(1):883–914, 2014. URL <http://doi.org/10.1016/j.spa.2013.09.012>.
- Umut Simsekli, Levent Sagun, and Mert Gurbuzbalaban. A tail-index analysis of stochastic gradient noise in deep neural networks. In Kamalika Chaudhuri and Ruslan Salakhutdinov, editors, *Proceedings of the 36th International Conference on Machine Learning*, volume 97 of *Proceedings of Machine Learning Research*, pages 5827–5837. PMLR, 09–15 Jun 2019. URL <http://proceedings.mlr.press/v97/simsekli19a.html>.
- Mahnoosh Tajmiriahi, Zahra Amini, Arsham Hamidi, Azhar Zam, and Hossein Rabbani. Modeling of retinal optical coherence tomography based on stochastic differential equations: Application to denoising. *IEEE Transactions on Medical Imaging*, 40(8):2129–2141, 2021. URL <http://doi.org/10.1109/TMI.2021.3073174>.
- Sayed Pouria Talebi, Simon J. Godsill, and Danilo P. Mandic. Filtering structures for  $\alpha$ -stable systems. *IEEE Control Systems Letters*, 7:553–558, 2023. URL <http://doi.org/10.1109/LCSYS.2022.3202827>.
- Lance A Waller. Does the characteristic function numerically distinguish distributions? *The American Statistician*, 49(2):150–152, 1995. URL <http://doi.org/10.1080/00031305.1995.10476133>.
- Xiaolong Wang, Jing Feng, Qi Liu, Yongge Li, and Yong Xu. Neural network-based parameter estimation of stochastic differential equations driven by Lévy noise. *Physica A: Statistical Mechanics and its Applications*, 606:128146, 2022. URL <https://doi.org/10.1016/j.physa.2022.128146>.
- Dixiong Yang, Hanshu Chen, Zeng Meng, and Guohai Chen. Random vibration and dynamic reliability analyses for nonlinear MDOF systems under additive excitations via DPIM. *Journal of Engineering Mechanics*, 147(12):04021117, 2021. URL [http://doi.org/10.1061/\(ASCE\)EM.1943-7889.0002029](http://doi.org/10.1061/(ASCE)EM.1943-7889.0002029).

## Appendix

### 5.1. Extended Literature Review

As mentioned in Section 1, Fourier duality gives us the intuition that characteristic function approaches to (1) may be both mathematically natural and computationally effective. We find validation of these ideas in recent work that addresses problems for (1) that are adjacent to but yet different from drift identification. For instance, Talebi et al. (2023) combined fractional-order calculus with a characteristic function framework to solve filtering problems for (1). One may be able to combine these ideas with those proposed here to pursue drift identification from noisy observations.

Our characteristic function evolution method is an alternative to the numerical solution of the fractional/non-local Fokker-Planck-Kolmogorov equation associated with (1). Suppose we take Fourier transforms of both sides of such an equation. We would then derive the differential version of the integral method that we pursue; in the literature, this differential equation is called the *spectral counterpart* to the Fokker-Planck-Kolmogorov or Einstein-Smoluchowski equation (Cottone, 2011; Alotta and Di Paola, 2014; Alotta and Di Paola, 2015; Di Matteo and Pirrotta, 2017; Di Paola and Alotta, 2020; Yang et al., 2021).

In much of this literature, time-dependent characteristic functions are used as intermediaries either to compute time-dependent densities (via inverse Fourier transform), or to establish connections between different types of evolution equations. Only Cottone (2011) derives a method that, as in our method, evolves the time-dependent characteristic function forward in time without any computations in physical space. Still, in the above literature, the full form of the drift and diffusion fields is assumed to be known *a priori* and the methods are used entirely for forward simulation.

In order for Fourier space methods to succeed in system identification, they should be able to compute the time-dependent characteristic function stably and accurately *even when the drift is approximated badly*, as may occur during the initial steps of an optimization loop. Our derivation, which begins with the Chapman-Kolmogorov equation in integral form (6) and ends with a closed-form integral equation (10) with no temporal or spatial derivatives, is designed to produce such a method.

### 5.2. Illustrative/Theoretical Properties

#### 5.2.1. GLOBAL BOUND

Using  $|e^{is^T \mathbf{x}}| = 1$  and  $p(\mathbf{x}) \geq 0$ , we have

$$|\psi(\mathbf{s})| = \left| \int_{\mathbf{x} \in \mathbb{R}^d} e^{is^T \mathbf{x}} p(\mathbf{x}) d\mathbf{x} \right| \leq \int_{\mathbf{x} \in \mathbb{R}^d} p(\mathbf{x}) d\mathbf{x} = 1.$$

Because  $\psi(\mathbf{0}) = 1$ , we see that  $\|\psi\|_\infty = 1$ . This global bound supports the strategy of using characteristic functions in a numerical scheme.

#### 5.2.2. CONCRETE EXAMPLE OF CHARACTERISTIC FUNCTION EVOLUTION

Let us focus attention on the one-dimensional ( $d = 1$ ) case. For one particular choice of  $f$  and  $G$ , we can use (8a) to solve for the time-dependent characteristic function of the solution of (1). We present this example to build intuition regarding (8a). In what follows, we use

$$\frac{1}{(2\pi)^d} \int_{\mathbf{y} \in \mathbb{R}^d} e^{i(\mathbf{s}-\mathbf{u})^T \mathbf{y}} d\mathbf{y} = \delta(\mathbf{s} - \mathbf{u}),$$



which was also used to compute the  $O(h^0)$  term in (9). Returning to  $\tilde{K}$  defined by (8b), we see that

$$\lim_{h \rightarrow 0} \tilde{K}(s, u) = \delta(s - u).$$

Now let us briefly switch gears. The following ordinary differential equation (ODE) is one of the easiest to solve:

$$\dot{x} = -x.$$

Given  $x(0) = x_0$ , the solution is  $x(t) = x_0 e^{-t}$ . The ODE has a globally stable, attracting fixed point at  $x = 0$ . This ODE is in fact a special, noiseless case of our Lévy SDE, with  $f(x) = -x$  and  $G(x) \equiv 0$ . The simplest way to reintroduce noise is to take  $G(x) = g > 0$ , a constant. In this case, the kernel becomes

$$\begin{aligned} \tilde{K}(s, u) &= \frac{1}{2\pi} \exp(-hg^\alpha |s|^\alpha) \int_{y=-\infty}^{\infty} e^{isy(1-h)} e^{-iuy} dy \\ &= \exp(-hg^\alpha |s|^\alpha) \delta(s(1-h) - u). \end{aligned} \tag{19}$$

With this kernel the evolution equation (8a) becomes

$$\psi_{n+1}(s) = \exp(-hg^\alpha |s|^\alpha) \psi_n(s(1-h)).$$

These relationships telescope, starting at  $\psi_n$  and going back to the initial condition  $\psi_0$ :

$$\begin{aligned} \psi_n(s) &= \exp(-hg^\alpha |s|^\alpha) \psi_{n-1}(s(1-h)) \\ \psi_{n-1}(s) &= \exp(-hg^\alpha |s|^\alpha) \psi_{n-2}(s(1-h)) \\ &\vdots \\ \psi_2(s) &= \exp(-hg^\alpha |s|^\alpha) \psi_1(s(1-h)) \\ \psi_1(s) &= \exp(-hg^\alpha |s|^\alpha) \psi_0(s(1-h)). \end{aligned}$$

Putting things together, we obtain

$$\psi_n(s) = \exp\left(-hg^\alpha |s|^\alpha \sum_{j=0}^{n-1} |1-h|^{j\alpha}\right) \psi_0(s(1-h)^n).$$

Let  $nh = t$  for some time  $t > 0$ . Fixing  $t$  and taking  $h \rightarrow 0$ , we obtain

$$\psi(s, t) = \exp(-g^\alpha |s|^\alpha \alpha^{-1} (1 - e^{-t\alpha})) \psi_0(e^{-t} s).$$

When  $\alpha = 2$ , this is the Fourier transform of the Ornstein-Uhlenbeck probability density function. When  $\alpha = 2$ , the SDE with drift  $f(x) = -x$  and constant  $G$  is indeed the Ornstein-Uhlenbeck SDE driven by standard Brownian motion. The upshot: we have used (8a) to solve this SDE for all  $\alpha$ , not only  $\alpha = 2$ .

### 5.2.3. CONCRETE EXAMPLE OF KERNEL EXPANSION

Continuing with the one-dimensional case, let us now consider  $f(x) = \sin x$  and  $G(x) \equiv g > 0$ . Using

$$\frac{1}{2\pi} \widehat{f}(k) = \frac{1}{2\pi} \int_{y=-\infty}^{\infty} e^{iky} \sin y \, dy = \frac{i}{2} [\delta(k-1) - \delta(k+1)]. \quad (20)$$

and

$$\frac{1}{2\pi} \widehat{f^2}(k) = \frac{1}{2\pi} \int_{y=-\infty}^{\infty} e^{iky} \sin^2 y \, dy = \frac{1}{4} [-\delta(k-2) + 2\delta(k) - \delta(k+2)], \quad (21)$$

we can compute the kernel expansion (9) up to second-order in  $h$ :

$$\begin{aligned} \tilde{K}(s, u) = \exp(-h|sg|^\alpha) & \left[ \delta(s-u) - \frac{1}{2}sh(\delta(s-u-1) - \delta(s-u+1)) \right. \\ & \left. - \frac{1}{8}s^2h^2(-\delta(s-u-2) + 2\delta(s-u) - \delta(s-u+2)) \right] \end{aligned} \quad (22)$$

Then using this kernel expansion in (8a), we obtain

$$\begin{aligned} \psi_{n+1}(s) = \exp(-h|sg|^\alpha) & \left[ \left(1 - \frac{1}{4}s^2h^2\right)\psi_n(s) \right. \\ & \left. - \frac{1}{2}sh(\psi_n(s-1) - \psi_n(s+1)) + \frac{1}{8}s^2h^2(\psi_n(s-2) + \psi_n(s+2)) \right] \end{aligned} \quad (23)$$

We can apply methods such as collocation to use (23) to evolve the characteristic function  $\psi_n$  forward in time starting from  $\psi_0$ . More generally, *if we know* the full form of an SDE, including the drift and diffusion functions, we may be able to derive from (8a) a customized numerical method for that particular SDE. While we do not pursue this in the present paper, we see scope for further numerical analysis of this approach as a method to solve Lévy-driven SDE.

Note that the coefficients that appear on the right-hand side of (23) are in fact Taylor expansions of Bessel functions of the first kind. Consider the exact kernel (8b) with  $f(y) = \sin y$  and apply the Jacobi-Anger expansion to obtain:

$$\begin{aligned} \tilde{K}(s, u) &= \frac{1}{2\pi} \exp(-h|sg|^\alpha) \int_{y=-\infty}^{\infty} e^{i(s-u)y} e^{ish \sin y} \, dy \\ &= \frac{1}{2\pi} \exp(-h|sg|^\alpha) \int_{y=-\infty}^{\infty} e^{i(s-u)y} \sum_{n=-\infty}^{\infty} J_n(sh) e^{iny} \, dy \\ &= \exp(-h|sg|^\alpha) \sum_{n=-\infty}^{\infty} J_n(sh) \delta(s-u+n) \end{aligned} \quad (24)$$

Now note that

$$\begin{aligned} J_0(sh) &= 1 - \frac{1}{4}s^2h^2 + O(h^4) \\ J_{\pm 1}(sh) &= \pm \frac{1}{2}sh + O(h^3) \\ J_{\pm 2}(sh) &= \frac{1}{8}s^2h^2 + O(h^4) \end{aligned}$$

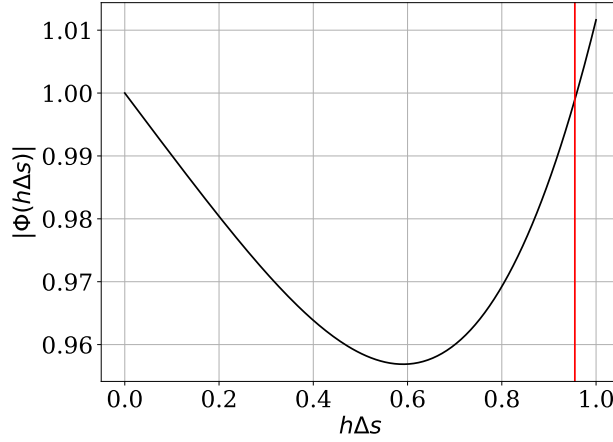


Figure 5: For  $g = 1/10$ , we plot  $|\Phi(h\Delta s)|$  as a function of  $h\Delta s$  and find that  $|\Phi(h\Delta s)| < 1$  for  $0 < h\Delta s < (h\Delta s)^*$  with  $(h\Delta s)^* \approx 0.955$  drawn in red. This gives a rough estimate of the stability region for (17).

For  $|n| \geq 3$ , the expansion of  $J_n(sh)$  begins with a term that is at least cubic in  $sh$ , and hence can be ignored for our purposes. Now substituting these Bessel function expansions into (24) and ignoring terms for which  $|n| \geq 3$ , we obtain precisely the same result as the kernel expansion (22).

### 5.3. On the Accuracy and Stability of the Fully Discrete Scheme (17)

To derive (17), we expanded in the time step  $h$  up to second order. Numerical analysis of the Euler-Maruyama method for SDE driven by Lévy  $\alpha$ -stable processes has established weak convergence at rates no better than  $O(h)$  (Jacod, 2004; Mikulevicius and Zhang, 2011). Our intuition is that because our approximation has  $O(h^3)$  truncation error, even after  $T/h$  time steps, the error of our approximation will be dominated by the error of the Euler-Maruyama method itself. As weak convergence is related to convergence of densities and characteristic functions, we expect to establish in future work that (10) converges at the same weak convergence rate of Euler-Maruyama.

We also see from (17) that the time step  $h$  always occurs together with the grid spacing  $\Delta s$ . The quantity  $h\Delta s$  can therefore be expected to play a role in accuracy and stability. One way to obtain a rough guide for stability is to analyze (17) in the scenario where  $\theta$  is a Kronecker delta,  $\mathbf{j}$  is a unit vector, and  $\psi_k$  is constant in space. In this case, (17) reduces to  $z_{k+1} = \Phi(h\Delta s)z_k$  with

$$\Phi(w) = e^{-wg^\alpha}(1 + iw - w^2/2).$$

Stability is assured for all  $w = h\Delta s$  such that  $|\Phi(w)| \leq 1$ . As one might expect, as the diffusion constant  $g$  increases, stability is guaranteed for larger values of  $w$ . For instance, when  $g = 1$ ,  $|\Phi(w)| \leq 1$  for all  $w \geq 0$ , with equality only at  $w = 0$ . For a more realistic value, such as  $g = 1/10$ , we find that  $|\Phi(w)| < 1$  for  $0 < w < 0.955$ , as depicted in Figure 5. At least in this idealized setting, stability is possible at reasonable values of  $h\Delta s$ , even though (17) is a fully explicit scheme.

#### 5.4. Adjoint Method Details

Here we detail an adjoint method designed to minimize the MMD loss  $\Lambda(\boldsymbol{\theta})$  (18) subject to the dynamics (17).

To simplify the notation, let  $\boldsymbol{\psi}_t \in \mathbb{C}^{(2M+1)^d}$  denote the complex vector that collects all entries of  $\psi(\mathbf{j}\Delta s, t; \boldsymbol{\theta})$ . Then the evolution equation (17) can be written in the following abstract form, with  $k = 0, \dots, \nu - 1$ :

$$\boldsymbol{\psi}_{t_j+(k+1)h} = \mathcal{P}(\boldsymbol{\theta})\boldsymbol{\psi}_{t_j+kh} \quad (25)$$

Here  $\mathcal{P}$  is our discrete-space, discrete-time propagator. One can obtain the  $(\mathbf{j}, \mathbf{j}')$ -th entry of  $\mathcal{P}$  by differentiating the right-hand side of (17) with respect to  $\psi_k(\mathbf{j}')$ .

With this, we can formulate the Lagrangian as

$$\mathcal{L}(\boldsymbol{\psi}, \boldsymbol{\lambda}, \boldsymbol{\theta}) = \frac{1}{2} \sum_{j=1}^N \left\| \boldsymbol{\psi}_j - \tilde{\boldsymbol{\psi}}_j \right\|^2 - \Re \sum_{j=0}^{N-1} \sum_{k=0}^{\nu-1} \boldsymbol{\lambda}_{t_j+(k+1)h}^\dagger \left( \boldsymbol{\psi}_{t_j+(k+1)h} - \mathcal{P}(\boldsymbol{\theta})\boldsymbol{\psi}_{t_j+kh} \right) \quad (26)$$

Here  $\boldsymbol{\lambda}_{t_j+(k+1)h} \in \mathbb{C}^{(2M+1)^d}$  is a Lagrange multiplier that enforces the dynamical constraint (25). Taking variations with respect to  $\boldsymbol{\psi}_j$ , we obtain

$$\begin{aligned} \delta \mathcal{L} &= \Re \sum_{j=1}^N (\boldsymbol{\psi}_j - \tilde{\boldsymbol{\psi}}_j)^\dagger \delta \boldsymbol{\psi}_{t_j} - \Re \sum_{j=0}^{N-1} \sum_{k=0}^{\nu-1} \boldsymbol{\lambda}_{t_j+(k+1)h}^\dagger \left( \delta \boldsymbol{\psi}_{t_j+(k+1)h} - \mathcal{P}(\boldsymbol{\theta}) \delta \boldsymbol{\psi}_{t_j+kh} \right) \\ &= \Re \sum_{j=1}^N (\boldsymbol{\psi}_j - \tilde{\boldsymbol{\psi}}_j)^\dagger \delta \boldsymbol{\psi}_j - \Re \sum_{j=0}^{N-1} \sum_{k=1}^{\nu} \boldsymbol{\lambda}_{t_j+kh}^\dagger \delta \boldsymbol{\psi}_{t_j+kh} + \Re \sum_{j=0}^{N-1} \sum_{k=0}^{\nu-1} \boldsymbol{\lambda}_{t_j+(k+1)h}^\dagger \mathcal{P}(\boldsymbol{\theta}) \delta \boldsymbol{\psi}_{t_j+kh} \end{aligned}$$

For optimality, we want  $\delta \mathcal{L}$  to vanish for all variations  $\delta \boldsymbol{\psi}$ . Note that the  $k = \nu$  terms are present only in the second sum on the right-hand side, not in the third sum. At  $k = \nu$ , since  $\nu h = \Delta t$ , we have  $t_j + \nu h = t_{j+1}$ . Therefore, at  $k = \nu$ ,  $\delta \boldsymbol{\psi}_{t_j+kh} = \delta \boldsymbol{\psi}_{t_{j+1}}$ . These variations vanish if we set

$$\boldsymbol{\lambda}_{t_j} = \boldsymbol{\psi}_j - \tilde{\boldsymbol{\psi}}_j, \quad (27)$$

for  $j = 1, \dots, N$ . The remaining variations vanish if we set

$$\boldsymbol{\lambda}_{t_j+kh}^\dagger = \boldsymbol{\lambda}_{t_j+(k+1)h}^\dagger \mathcal{P}(\boldsymbol{\theta}). \quad (28)$$

We recognize (27) as the final condition for (28), the backward-in-time adjoint equation corresponding to the forward dynamics (25).

We can now outline a procedure to compute  $\nabla_{\boldsymbol{\theta}} \Lambda$ , the gradient of the loss function with respect to the model parameters. Given a trial value of  $\boldsymbol{\theta}$ , we solve (25) forward in time using the empirical characteristic functions at times  $t_j$  (for  $j = 0, \dots, N - 1$ ) as initial conditions—see (11) and surrounding discussion. We then solve (28) backward in time with final condition (27). This enables us to evaluate

$$\nabla_{\boldsymbol{\theta}} \mathcal{L} = \Re \sum_{j=0}^{N-1} \sum_{k=0}^{\nu-1} \boldsymbol{\lambda}_{t_j+(k+1)h}^\dagger \nabla_{\boldsymbol{\theta}} \mathcal{P}(\boldsymbol{\theta}) \boldsymbol{\psi}_{t_j+kh}. \quad (29)$$

That this gradient equals  $\nabla_{\boldsymbol{\theta}} \Lambda$  is a consequence of the Lagrange multiplier theorem. To compute the right-hand side (29), it suffices to have a method to multiply the gradient  $\nabla_{\boldsymbol{\theta}} \mathcal{P}(\boldsymbol{\theta})$  by a vector

$\psi$ . We obtain such a method by differentiating the right-hand side of (17) with respect to  $\theta$ . This yields

$$\frac{\partial}{\partial \theta_q^r} [\mathcal{P}(\theta) \psi_t]_{\mathbf{j}} = e^{-h\Delta s |\mathbf{j}^T \mathbf{g}|^\alpha} \left[ i(h\Delta s) j_q \psi_t(\mathbf{j} + \mathbf{r} n_L) - (h\Delta s)^2 \sum_{\mathbf{k} \in \mathcal{K}} j_q (\theta^{\mathbf{k}-\mathbf{r}})^T \mathbf{j} \psi_t(\mathbf{j} + \mathbf{k} n_L) \right] \quad (30)$$

### 5.5. Implementation Details

For all tests, we use our own Python implementation of the characteristic function evolution method and associated adjoint method. We have implemented the methods using Numba (Lam et al., 2015), making use of both JIT, just-in-time compilation, and CUDA, enabling us to run our code on GPUs. All Euler-Maruyama runs (to generate training data) were carried out using Mathematica. We are in the process of making source code available at the URL <https://github.com/hbhat4000/levyL4DC>.

When we optimize in one-dimensional problems, we set the optimization tolerances to  $10^{-9}$ . For two-dimensional problems, we set the tolerances to  $10^{-3}$ .

**One-Dimensional Vector Fields.** To generate trajectories, we applied Euler-Maruyama with a time step of  $10^{-3}$  for 4001 steps, but only saved the solution every 100 steps.

When we apply the characteristic function evolution method (17), we use the following parameters:  $L = 2$ ,  $M = 1028$ , and  $n_L = 8$ . This implies that we track characteristic functions at  $2M + 1 = 2049$  points in Fourier space, with  $\Delta s = 0.0625$ .

**Two-Dimensional Trigonometric Vector Fields.** To generate trajectories corresponding to the trigonometric vector fields with results plotted in Figure 2, we applied Euler-Maruyama with time step  $10^{-4}$  for 400001 steps, saving the solution every 4000 steps.

For each trajectory, the initial condition is  $\mathbf{X}_0 = (X_{0,0}, 0)$  where  $X_{0,0}$  is drawn from a normal distribution with mean 0 and standard deviation  $1/3$ .

To conserve memory, we track the characteristic function on a coarse grid with only  $2M + 1 = 65$  points in Fourier space per dimension. We set  $L = 2$  and  $n_L = 4$  so that  $\Delta s = 0.125$ .

**Two-Dimensional Polynomial Double Well Vector Field.** Initial conditions  $\mathbf{X}_0$  were chosen as described above for two-dimensional trigonometric vector fields. The Euler-Maruyama runs were also conducted as above, except that the solution was saved every  $10^4$  steps.

We again track the characteristic function on a coarse grid with only  $2M + 1 = 65$  points in Fourier space per dimension. We set  $L = 2$  and  $n_L = 4$  so that  $\Delta s = 0.125$ .

Note that we retain the  $\mathcal{L}^1$  regularization term  $\mu \|\theta\|_1$  with  $\mu = 1$ . We seek to promote sparsity for this polynomial vector field because when we examine  $\tilde{\mathbf{f}}(\mathbf{x})$ , we see that  $\tilde{f}_1$  depends only on  $x_2$  and  $\tilde{f}_2$  depends only on  $x_1$ . Hence the true  $\tilde{\theta}$  coefficients will be sparse.

**Maier-Stein Polynomial Vector Field.** Initial conditions  $\mathbf{X}_0$  were chosen from an equispaced  $10 \times 10$  grid on the square  $[-1, 1]^2$ . The Euler-Maruyama runs used a time step of  $10^{-4}$  for 100001 steps. The solution was saved every 10000 steps.

We again track the characteristic function on a coarse grid with only  $2M + 1 = 65$  points in Fourier space per dimension. We set  $L = 2$  and  $n_L = 8$  so that  $\Delta s = 0.0625$ .

We keep the  $\mathcal{L}^1$  regularization term  $\mu \|\theta\|_1$  but relax  $\mu$  to 0.1.

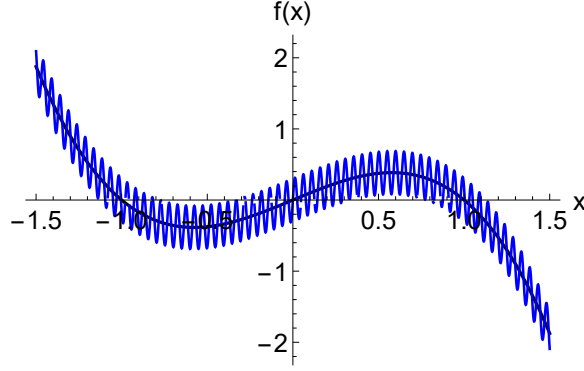


Figure 6: Ground truth  $\tilde{f}(x) = x - x^3$  (in black) together with Fourier series approximation computed using exact Fourier coefficients (31) with  $J = 256$  modes (in blue).

### 5.6. Analyzing the Error for the One-Dimensional Polynomial Double Well

Here we continue the discussion of the right-most plot in Figure 1, corresponding to the true (black)  $\tilde{f}(x) = x - x^3$  and the estimated (red)  $f$ .

For  $|x| > 2$  (not plotted), the two curves diverge; the mean absolute error between estimated  $\tilde{\theta}$  and true  $\theta$  coefficients is large. We hypothesize that this occurs because (i) we are trying to model a polynomial vector field  $\tilde{f}$  using a Fourier series  $f$ , (ii)  $J = 16$  Fourier modes is insufficient to capture the behavior of this polynomial  $\tilde{f}$ , and (iii) the training data does not adequately explore phase space for  $|x| > 2$ .

Let us focus on reason (i) above. The Fourier coefficients  $\tilde{\theta}$  corresponding to the ground truth field  $\tilde{f}$  satisfy  $\tilde{\theta}_0 = 0$  and for  $j \neq 0$ ,

$$\tilde{\theta}_j = -\frac{2i(-1)^j((4\pi^2 - 1)j^2 - 24)}{j^3} \quad (31)$$

It is clear that these coefficients decay to zero slowly, e.g.,  $|\tilde{\theta}_j| \sim O(1/j)$  for  $|j| \gg 1$ . Suppose we use these *exact* Fourier coefficients in (13) with  $J = 256$ . In Figure 6, we have plotted the resulting Fourier series approximation (in blue) together with the ground truth  $\tilde{f}$  (in black). Note the presence of oscillations that lead to an overall *worse* approximation of  $\tilde{f}$  than we saw in the right-most panel of Figure 1. In short, the result we obtained in the right-most panel of Figure 1 with  $J = 16$  modes should be viewed as quite good, especially considering that  $\alpha = 1$  in the SDE (1).

With this in mind, we introduce another way to measure error, akin to pointwise-in-time test set error. Using the true  $\tilde{f}$ , we generate a set of trajectories  $\tilde{\mathcal{T}}$  starting from  $X_0 = 0$ . For this same initial condition, we then recompute the trajectories with (i) the true  $\tilde{f}$ , resulting in  $\mathcal{T}'$ , and (ii) the estimated  $\tilde{f}$ , resulting in  $\mathcal{T}$ . We then compute the median of median absolute errors (MMAE) and median of interquartile ranges (MIQR) between  $\tilde{\mathcal{T}}$  and  $\mathcal{T}$ , a natural measure of how well our learned  $f$  predicts trajectories. We compare this against the MMAE and MIQR between  $\tilde{\mathcal{T}}$  and  $\mathcal{T}'$ , the error we would have obtained had our learned  $f$  *exactly matched* the ground truth  $\tilde{f}$ . Because (1) is stochastic, this latter error will never be zero.

Carrying this out for 1000 trajectories, we find that for 25 trajectories, we obtain overflow errors from the ground truth polynomial vector field  $\tilde{f}$  in the  $\alpha = 1$  (Cauchy noise) case. This does not happen with the Fourier representation  $f$ ; we conjecture this is because  $\tilde{f}$  is not Lipschitz while  $f$  is. Eliminating the 25 trajectories with overflow errors, we obtain a MMAE of 0.910 and MIQR of 0.912 for the comparison between  $\tilde{\mathcal{T}}$  and  $\mathcal{T}$ . This is not far from the MMAE of 0.723 and MIQR of 0.800 for the comparison between  $\tilde{\mathcal{T}}$  and  $\mathcal{T}'$ .